Title

Feasibility of FDEM cross-dipole and TDEM loop sources for monitoring CO2 at the Kemper CarbonSAFE site

Authors

Kohnke, Colton
Li, Yaoguo
Hammack, Richard W
et al.

Publication Date

2023-07-01

DOI

10.1016/j.ijggc.2023.103918

Peer reviewed

International Journal of Greenhouse Gas Control 127 (2023) 103918

Contents lists available at ScienceDirect

International Journal of Greenhouse Gas Control

journal homepage: www.elsevier.com/locate/ijggc

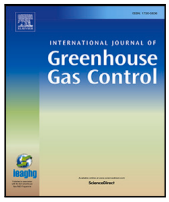

Feasibility of FDEM cross-dipole and TDEM loop sources for monitoring CO_2 at the Kemper CarbonSAFE site

Colton Kohnke [a,*], Yaoguo Li [b], Richard W. Hammack [a], David Alumbaugh [c]

[a] U.S. Department of Energy, National Energy Technology Laboratory, 626 Wallace Rd, 15236, Pittsburgh, PA, USA
[b] Colorado School of Mines, Center for Gravity, Electrical, and Magnetic Studies, 1500 Illinois St., 80401, Golden, CO, USA
[c] Lawrence Berkeley National Laboratory, Earth and Environmental Sciences, 1 Cyclotron Road, 94720, Berkeley, CA, USA

ARTICLE INFO

Keywords:
Electromagnetics
Forward-modeling
Monitoring
Carbon storage

ABSTRACT

Electromagnetics has been shown to be a viable tool to monitor CO_2 plumes embedded in saline reservoirs. However, the majority of studies focus on measuring the electric field, which requires cumbersome equipment in the field and it is difficult to install permanent measurement stations. Magnetic field receivers offer an opportunity to reduce the form factor of the survey and increase the mobility by utilizing upcoming technologies, such as drones. We explore the use of frequency-domain electric dipole sources, and time-domain loops with a focus on measuring the secondary magnetic field at the surface for a conceptual injection scenario based on the Kemper CarbonSAFE site. We find that electric dipole sources give a response above the sensitivity of current sensor technology and, therefore, be a viable tool for CO_2 monitoring. The time-domain loop source does provide fields that are useful for determining the location of the CO_2 plume, however the field magnitude is below the sensitivity of the current generation of instruments. To explore the use of a potential borehole receiver we generate a map of the magnetic field at depth to explore potential borehole placement for monitoring efforts. Finally, we limit the spatial extent of the electric dipole survey to a single parcel of land to help understand how the fields change with survey geometry. We find that the shape of the secondary fields change slightly with the small transmitter, but are still measurable provided that the cultural noise at the site is low. Thus, we conclude that at the Kemper site a frequency-domain cross-dipole source with magnetometer receivers is suitable to monitor the expansion of the CO_2 plume in the saline reservoir, even with a limited transmitter footprint on the surface.

1. Introduction

Storing supercritical carbon dioxide (CO_2) in geologic formations is a way to reduce CO_2 in the atmosphere and mitigate the effects of climate change. The storage site needs to be monitored to ensure the CO_2 does not move out of the geologic formation. Regularly scheduled monitoring efforts are also needed to satisfy safety and regulatory requirements for up to 80 years post injection (Benson et al., 2005). Geophysics, the most relevant methods being seismic, gravity, and electromagnetics, can play a vital role in these monitoring efforts. Unfortunately, the cost of repeated surveys can make operating a CO_2 storage site expensive, especially when using the seismic method. A way to reduce the cost is to setup permanent monitoring sites using low-cost geophysical methods in order to rapidly gain insight to, and make near real-time decisions about, the CO_2 storage site.

One potential location for a storage site is at the Kemper County CarbonSAFE site in Mississippi. The local power station produces and captures CO_2, which will then be transported a few miles to the injection site where the CO_2 would be stored underground in a saline reservoir at depth. The short distance provides an enormous benefit to cost-saving measures. Smith et al. (2021) estimates that the cost of transporting and storing CO_2 at a standard site is on the order of $11 USD per tonne CO_2 with 30% of the cost attributed to transportation over long distances. Monitoring efforts are estimated to cost an additional $6 USD per tonne CO_2. While these costs are dependent on factors such as the local geology, transportation distance, and injection rate, the proximity of the Kemper CarbonSAFE site to where the CO_2 is captured and the cost saving of a permanent monitoring site can help reduce the cost significantly and make CO_2 storage operations more affordable. Studies at the North Dakota CarbonSAFE project (Barajas-Olalde et al., 2021) suggest that electromagnetics is worth exploring for monitoring carbon sites, however each site has unique geology

* Corresponding author.
E-mail addresses: colton.kohnke@netl.doe.gov (C. Kohnke), ygli@mines.edu (Y. Li), richard.hammack@netl.doe.gov (R.W. Hammack), dlalumbaugh@lbl.gov (D. Alumbaugh).

https://doi.org/10.1016/j.ijggc.2023.103918
Received 12 October 2022; Received in revised form 8 May 2023; Accepted 20 May 2023
Available online 6 June 2023

and a separate feasibility study must be undertaken before adding electromagnetics to the monitoring strategy.

To monitor the Kemper CarbonSAFE site, we propose using electromagnetic methods with an emphasis on the information gained by including magnetic field measurements. By focusing on magnetic field receivers, we avoid the equipment necessary to measure the electric field. Recent advances in magnetic sensor technology allow for deep soundings with low internal levels of noise using SQUID magnetometers (Arai, 2003), and provides the ability to translate to other new technologies, such as drone-based receivers (Stoll, 2021).

There are few studies that examine the role of EM in CO_2 monitoring, though this line of research has recently seen an increase in publications. Traditionally the EM problem focuses on detecting and defining conductors in a resistive media, such as in mineral exploration applications. The CO_2 monitoring problem, however, is focused on delineating a resistor that represents the plume of supercritical CO_2 inside a saline aquifer. In the time-lapse sense, instead of defining a conductor, one defines how a conductor becomes more resistive as CO_2 is injected into the subsurface. Klara et al. (2004), Hoversten and Gasperikova (2005), and Gasperikova and Hoversten (2006) are likely the first studies to consider the use of geophysics, and non-seismic methods, to assist carbon capture, utilization, and storage (CCUS) efforts. These studies find that geophysics can contribute over the life of the storage site and offer viable methods for characterizing the site prior to injection, monitoring the CO_2 during injection, and evaluating the site post-injection.

Recent studies explore different source–receiver configurations to aid in monitoring efforts. Streich et al. (2010) shows that controlled-source magnetotellurics (CSMT) can detect a resistive disk in the subsurface by measuring the electric fields the surface or depth. Zhdanov et al. (2013) shows that borehole-to-surface EM (BSEM) is able to monitor deep reservoirs using electric bipole sources and receivers. Börner et al. (2015) explores a fictitious monitoring scenario using BSEM using horizontal electric dipole (HED) and vertical magnetic dipole (VMD) sources and find that while the HED source performs better, it is still possible to monitor the scenario using a VMD source. Börner and Spitzer (2013) expands this study to include scenarios with the CO_2 leaking into a near-surface freshwater aquifer. Beka et al. (2017) uses inversion to combine magnetotellurics (MT) and transient EM (TEM) measurements to resolve conductive and resistive blocks that represent the saline and CO_2 reservoirs. The results suggest that the methods are unable to resolve deep resistive units, however, this study neglects to consider a scenario with a resistor embedded in a conductor, which is more representative of the CCUS monitoring challenge. Kang et al. (2012), Ayani et al. (2019), and Bhuyian et al. (2011) all consider using marine CSEM to monitor offshore CO_2 injection, and that by using long receiver offsets (greater than 7 km) the reservoir is detectable at 2 km depth. Finally, Puzyrev (2019) shows that the problem of imaging a CO_2 plume can be approached using machine learning techniques and a BSEM configuration.

While the literature suggests that the best method of monitoring is to place the sources and receivers near the CO_2 plume in the subsurface, this method is limited to locations with existing boreholes that may not be readily accessible to accept downhole tools. Instead, methods which charge the borehole from the surface, as in McAliley et al. (2019), Krahenbuhl et al. (2019), and MacLennan (2022), show a promising method for monitoring, but are also limited to where boreholes exist in the field. The literature also prefers HED type sources as they induce horizontal and vertical currents in the subsurface. The HED source is not a significant issue in the field, except they are often paired with electric field receivers, which are cumbersome to install in the field due to long cables, dense vegetation, and terrain. Animals tend to chew the receiver cables, making permanent installations difficult. Electric field receivers are not able to move location easily in the case of unexpected reservoir behavior. VMD sources are readily dismissed in literature due to the fact that only horizontal currents are induced during such surveys, making it difficult to delineate vertical conductivity structures in the subsurface. However, as Börner et al. (2015) shows, difficult is not impossible, and a VMD source warrants a re-examination at the Kemper CarbonSAFE site due to its low cost and ease to deploy in the field. To this end, we examine the use of cross-dipole and time-domain EM sources at the Kemper CarbonSAFE site, with a focus on measuring the magnetic field for survey mobility.

This paper is organized as follows: first, we examine the geologic context of the Kemper CarbonSAFE site and derive a geo-electric model. Next, we examine the constraints and assumptions of the geophysical equipment. Finally, we present the modeling results and give recommendations to the monitoring efforts.

2. Geologic overview of Kemper County, Mississippi

Kemper County, Mississippi is located on the eastern edge of the state along the border shared with Alabama. The primary geologic studies in the region are described by Hughes (1958) and Brown (1960). The regional geology is part of the Central Gulf Coastal Plain and is underlain by sedimentary formations of sand, clay, marl, limestone, and chalk ranging from Jurassic to Recent in age. The sediments in this geologic region are lacking in uniformity and each basin is characterized by its local sediments — representing many types of depositional environments and making regional correlation difficult between basins. The primary mechanism of deposition in the region were the sea and streams from the surrounding highland areas. The sediment units dip gently seaward (to the southwest and south) at a rate that is generally less than half a degree. For reference, this dip corresponds to about 10 meters per kilometer, so the local geology in Kemper County can be treated as a 1D “layer-cake” from a geophysical perspective.

The area of interest for CO_2 storage in Kemper County is shown in Fig. 1. The northern section shows the power plant, where CO_2 is planned to be captured, located near the site of the MPC 10-4 well. The MPC 32-1 and MPC 19-2 wells are the sites of proposed CO_2 injection. The concentric circles around the MPC 32-1 well represents 2 and 5 km of CO_2 plume expansion at depth and give an area to consider while designing the surface surveys. The irregular polygon to the South-East of MPC 32-1 represents a potential area to setup an electromagnetic transmitter due to known land access constraints. The aerial photograph suggests the area is heavily forested with few clearings, making land-based surveys difficult. To cover more area and utilize the available land area, one may deploy the transmitter inside the irregular polygon and drone or airborne based surveying methods for the receivers.

Fig. 2 shows the generalized stratigraphic column for Kemper County. The geologic units of interest for CO_2 injection and storage are the Lower Tuscaloosa Group, the Washita–Fredricksburg interval, and the Paluxy Formation (Dockery III and Thompson, 2016). The Lower Tuscaloosa Group is characterized by the Massive Sand and Dantzler Sand units deposited along the Cretaceous coast line. The Washita–Fredricksburg interval is characterized by sand, limestone, and mudstone in the lower section and shale and sands in the upper section. Finally, the Pauluxy formation contains alternating sequences of fine-sand and shale. These three sandstone intervals combined are on the order of 330 m thick with an average porosity of 30% and a permeability of 16 Darcys. The sandstone layers are found to be saturated with brine. There is another near-surface sandstone unit at the base of the Naheola Formation which is filled with brine. However, this unit is not deep enough to support supercritical CO_2 injection.

The reservoirs are confined by the Tuscaloosa marine shale and the shale intervals at the top and base of the Washita–Fredricksburg interval. The Selma Group (limestone and chalk) and Porters Creek (clay) also act as shallower seals for the reservoir. The shale that make up these seals are described as soft and pliable, making them difficult to fracture. The permeability of the shale units are in the nanoDarcy range

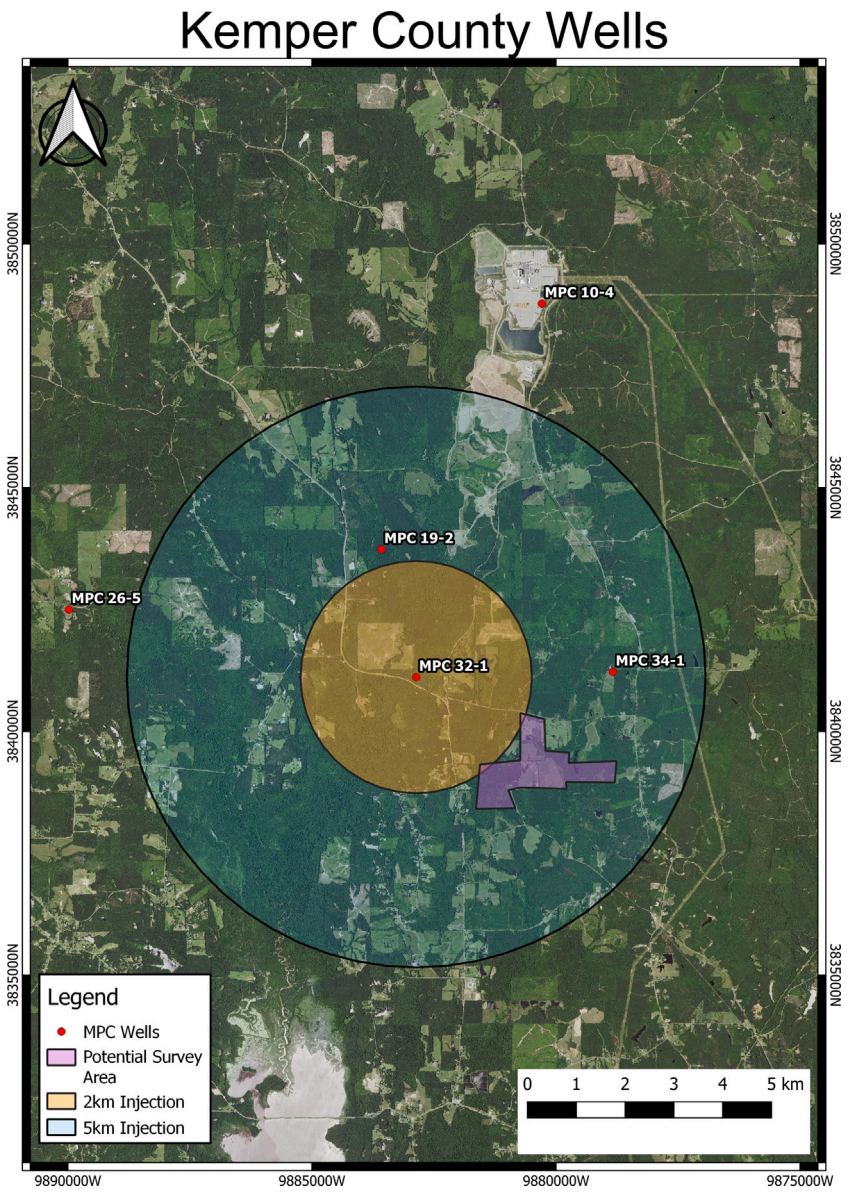

Fig. 1. Local map of wells at Kemper County. The local power station is located at MPC 10-4, and a possible injection well is located at MPC 32-1. The 2 and 5 km CO_2 plume expansions, and a potential area for electromagnetic surveys are shown for reference.

and the thickness of the units severely limit the potential for vertical migration and leakage (Riestenberg, 2018). The seals are also found to be continuous over the county and surrounding area from geophysical data and well-logs.

2.1. Building a conductivity model

To determine a baseline geo-electric model of the site we use the induction logs from six wells in the area including the MPC 26-5, 32-1, 34-1, and 10-4 wells shown in Fig. 1. From the logs we construct the 1D conductivity model in Fig. 3. The logs start at the top of the Selma Group and extend to the middle of the Paluxy Formation, so the units above and below this interval are assumed to be 0.5 Ωm. Overall, the geologic section is found to be fairly conductive from an electromagnetics standpoint, likely due to the brine saturation. The electromagnetic source dissipates quickly in conductive regimes, but with proper survey techniques, this limitation can be overcome and an image of the subsurface can be obtained.

To approximate the time-lapse conductivity of the CO_2 reservoir, we first start with Archie's equation (Archie, 1942)

$$\rho = \alpha \phi^{-m} S_w^{-n} \rho_w, \tag{1}$$

where ρ is the composite resistivity of the rock, ϕ is the rock porosity, S_w is the water saturation of the rock, and ρ_w is the resistivity of the formation water. The exponents m and n are cementation and saturation factors, respectively. Values for n and m for unknown cementation and saturation factors are assumed to be 2 (Keller, 1988). The leading α is a proportionality constant, and is typically assumed to be unitary.

When CO_2 is added to the system, the CO_2 saturation can be expressed in terms of water saturation as

$$S_{CO_2} = 1 - S_w = 1 - \left(\alpha \rho_w \phi^{-m} \rho^{-1}\right)^{\frac{1}{n}} \tag{2}$$

To compute the bulk resistivity of the reservoir with CO_2 added, we assume the pore-space is filled with either CO_2 or brine, and the bulk resistivity becomes

$$\rho = \alpha (1 - S_{CO_2})^{-n} \phi^{-m} \rho_w. \tag{3}$$

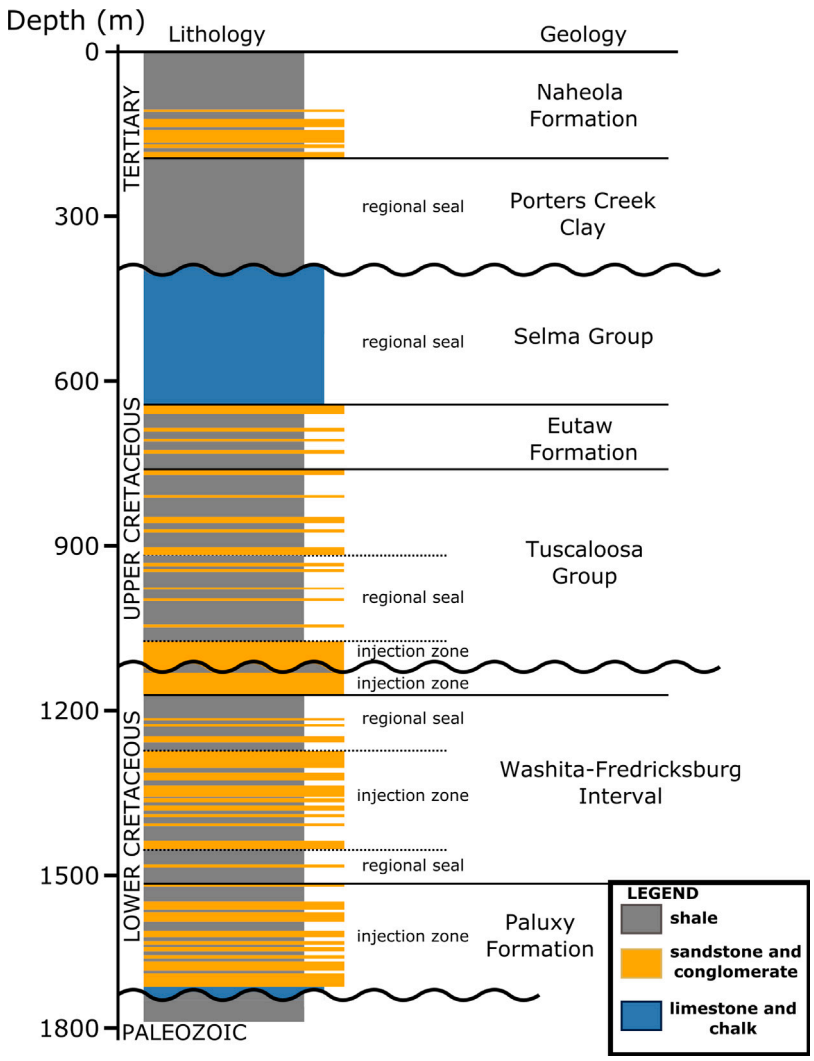

Fig. 2. Generalized stratigraphic column of Kemper County, MS.
Source: Modified from Hughes (1958).

We choose a value of 2 for the saturation index and cementation factor (n and m) (Onishi et al., 2006). The sandstone is assumed to be fully saturated initially, and the saturation of CO_2 after injection is assumed to be 80%. The average porosity of the injection units has been measured as 30%. From the well logs, ρ in the saline reservoirs is 3.5 Ωm when $S_w = 1$, which yields a ρ_w of 3.15 Ωm. Therefore at a saturation of 80%, the bulk resistivity of the CO_2 flooded section is then approximated as 87.5 Ωm. Eq. (1) was originally derived empirically for clean sandstone units, and while the sandstone units at Kemper do have some thin shale expressions, they are rare in the core samples that were collected onsite. Modifications for Archie's equation must be made if the host rock is conductive or if the formation water is non-saline, though due to standard rock conductivity for sandstone (Palacky, 1988) and the well logs indicating the presence of a strong conductor in the sandstone units, we do not believe either scenario is present. Therefore, Eq. (1) is an approximation to the bulk resistivity, but it is a reasonable approximation in the case of the Kemper site.

The volume of the CO_2 in the subsurface will depend on the temperature, pressure, porosity, and permeability of the reservoir. As an approximation, we choose to base the plume expansion on the modeling study in the Illinois Basin by Zhou et al. (2009). This study suggests that for a single well, injecting 5 Mt CO_2 annually over 50 years, the total radius of the CO_2 is approximately 3 km. The majority of the expansion comes from the first 5 years of injection, where the plume expands to 750 m in radius. The plume therefore expands at a rate of 150 m per year if we assume the expansion is linear for the first 5 years. As a further approximation, we assume the CO_2 plume expands as a 3D disk in each reservoir layer rather than a cone shape. We make this approximation to more easily control the volume and horizontal extent of the CO_2 plume in the reservoir layers.

We construct geologic model representing projections for three epochs of injection, shown in Fig. 4. The disk expands from 150 m to 750 m radius in the subsurface between the first and third epochs of injection and approximate 1, 3, and 5 years of injection. The models assume an optimistic 80% CO_2 saturation for the plume zone throughout, although the saturation will be highest at the injection zone and decrease radially away from the well (Zhang et al., 2015). A lower expected CO_2 saturation will have a lower conductivity contrast with the saline reservoir and measured EM response. Therefore, one must consider local geology and reservoir simulations when determining if EM is appropriate for monitoring specific sites. To approximate a depth of investigation using electromagnetics, we can use the skin depth equation,

$$\delta \approx 503\sqrt{\frac{1}{f\sigma}}, \tag{4}$$

where f is frequency, and σ is a bulk conductivity of the subsurface. Using a bulk conductivity of 0.25 S/m and frequencies of 0.1–10 Hz gives a skin depth of 0.3 km for 10 Hz, and 3.1 km for 0.1 Hz, meaning

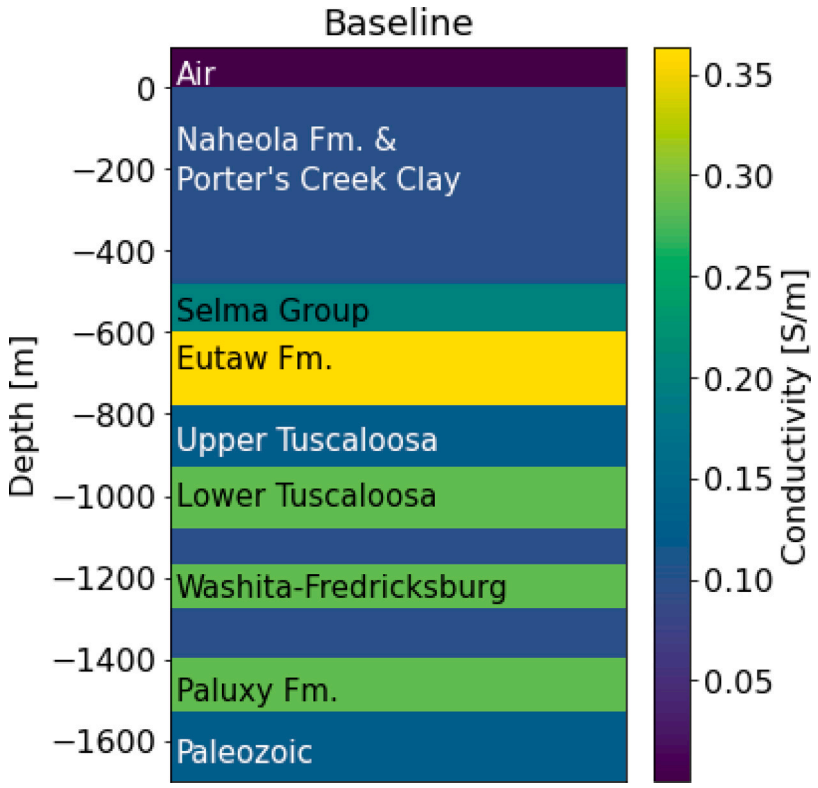

Fig. 3. Baseline conductivity model derived from induction logs at the well locations.

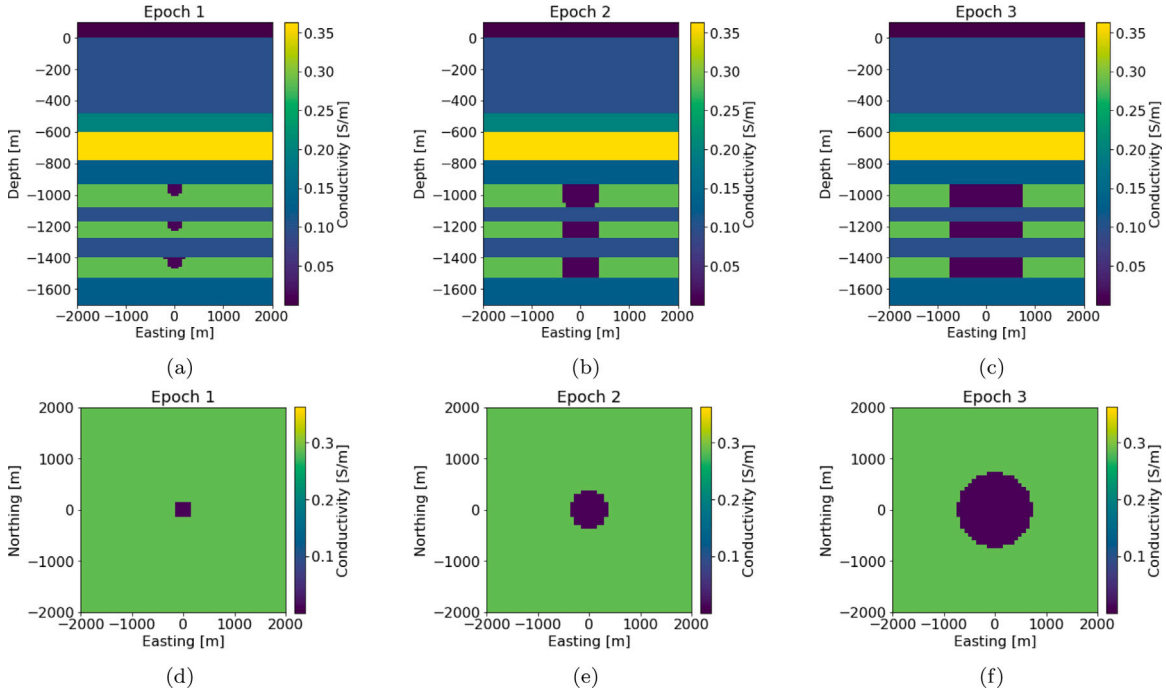

Fig. 4. Final 3D conductivity models for epoch 1 (left), epoch 2 (middle), and epoch 3 (right) in cross-section view (top), and plan view (bottom).

these frequencies should be able to detect conductivity changes at the reservoir depth. Additionally, it should be noted that skin depth is an imperfect analog to depth of investigation, as a stronger transmitter and more sensitive receivers can overcome the field strength decay predicted by skin depth.

3. Current EM equipment

Geophysical equipment to measure the electromagnetic fields has come a long ways in the last 50 or so years. Most systems make use of induction coils or fluxgate magnetometers to measure the magnetic

flux density or its time derivative. However, systems based on these receiver types are susceptible to relatively high levels of internal and external noise. As geophysical targets have become smaller and deeper, the signal to resolve the targets has likewise become smaller, and the noise must decrease to match. Superconducting Quantum Interference Devices (SQUIDs) have been proven to have low levels of internal noise ($\approx$50 fT/$\sqrt{\text{Hz}}$) and with a sensitivity floor below 0.1 pT.

Transmitters have likewise seen a similar evolution in engineering. Time-domain transmitter loops have upgraded from delivering approximately 1.5 kW of power and a maximum 10 A of current to delivering 18–80 kW of power and upwards of 80 A of current while maintaining a turn-off time in the hundreds of microseconds. Frequency-domain electric dipole transmitters are currently capable of similar feats and are able to support 25 kW of power and 30–60 A of current depending on the geology, and a source signal of 0.125–1 Hz. The physical size of the transmitters have also increased, increasing the source dipole moment and inducing field accordingly. It is not uncommon to have transmitter loops or electric dipole transmitters of multiple kilometers in length.

The studies presented in this paper incorporate a "best case scenario" for the transmitters and receivers. We consider a sensitivity floor of 0.1 pT to be obtainable for the measured magnetic flux density. We do not consider the internal noise of the instrument, as it is considered to be far below the signal. We also do not consider the cultural noise at the site, as it is unknown at this time. We consider a transmitter with a current up to 80 A, but present results normalized by current as to make inferences about a general transmitter.

4. Finite-volume EM modeling

To simulate the magnetic fields produced by the surveys over the proposed geologic models, we start with Maxwell's equations in the frequency domain

$$\begin{aligned} \nabla \times \mathbf{E} + i\omega\mathbf{B} &= \mathbf{S}_m \\ \nabla \times \mathbf{H} - \mathbf{J} - i\omega\mathbf{D} &= \mathbf{S}_e \\ \nabla \cdot \mathbf{B} &= 0 \\ \nabla \cdot \mathbf{D} &= \rho_f \end{aligned} \tag{5}$$

where $\mathbf{E}$ is the electric field (V/m), $\mathbf{D}$ is the electric displacement (C/m^2), $\mathbf{J}$ is the electric current density (A/m^2). The magnetic components are then $\mathbf{B}$ as the magnetic flux density (T), and $\mathbf{H}$ as the magnetic field (A/m). $\mathbf{S}_m$ and $\mathbf{S}_e$ are the magnetic (V/m^2) and electric (A/m^2) source terms, and ρ_f is the free charge density (Ωm). Constitutive relationships relate the fields and fluxes through physical properties of the material as

$$\begin{aligned} \mathbf{J} &= \sigma\mathbf{E} \\ \mathbf{B} &= \mu\mathbf{H} \\ \mathbf{D} &= \varepsilon\mathbf{E}, \end{aligned} \tag{6}$$

where σ is the electrical conductivity (S/m), μ is the magnetic permeability (H/m), and ε is the dielectric permittivity (F/m). It is common in geophysical problems involving geologic bodies and interpretation to have μ and ε assume their free-space values of $\mu_0 = 4\pi \times 10^{-7}$ H/m and $\varepsilon_0 \approx 8.85 \times 10^{-12}$ F/m. However, for problems with strong conductors, such as steel-cased wells or other infrastructure, this approximation will not necessarily hold.

Maxwell's equations can be simplified by using a quasi-static approximation that assumes displacement currents are negligible when $\sigma \gg \omega\varepsilon$, giving

$$\begin{aligned} \nabla \times \mathbf{E} + i\omega\mathbf{B} &= \mathbf{S}_m \\ \nabla \times \mathbf{H} - \mathbf{J} &= \mathbf{S}_e. \end{aligned} \tag{7}$$

The maximum frequencies of the geophysical surveys we investigate in this paper are on the order of 10 Hz. The conductivity of the subsurface varies logarithmically, with igneous and limestone rocks having a low floor at approximately 1e−5 S/m. The air layer in the model is typically chosen to have a constant conductivity between 1e−7 and 1e−9 S/m. Regardless, the quasi-static approximation holds for the frequencies we are interested in exploring.

Finally, we can manipulate Eq. (7) using the constitutive relations in equation Eq. (6) to put the equations in terms of two fields, either $\mathbf{E}$ and $\mathbf{B}$ or $\mathbf{H}$ and $\mathbf{J}$. The E-B formulation is more direct to the fields we are interested in solving for, so we choose to write

$$\begin{aligned} \nabla \times \mathbf{E} + i\omega\mathbf{B} &= \mathbf{S}_m \\ \nabla \times \mu_0^{-1}\mathbf{B} - \sigma\mathbf{E} &= \mathbf{S}_e. \end{aligned} \tag{8}$$

Eq. (8) is then discretized onto a 3D mesh consisting of rectangular cells where $\mathbf{E}$ exists on cell edges, $\mathbf{B}$ exists at the center of cell faces, and σ exists at cell centers, and is written as

$$\begin{aligned} \mathbf{C}\mathbf{e} + i\omega\mathbf{b} &= \mathbf{s}_m \\ \mathbf{C}^\top \mathbf{M}^f_{\mu_0^{-1}}\mathbf{b} - \mathbf{M}^e_\sigma\mathbf{e} &= \mathbf{M}^e\mathbf{s}_e. \end{aligned} \tag{9}$$

The lowercase $\mathbf{e}$, $\mathbf{b}$, and $\mathbf{s}$ are the discretized forms of their uppercase counterparts. The matrix $\mathbf{C}$ performs the curl operator and moves quantities from the cell edge to the center of cell faces. The transpose of $\mathbf{C}$ performs the curl while moving quantities from center of cell faces to the cell edges. The matrix $\mathbf{M}$ then interpolates the quantity denoted by the subscript to the location denoted by the superscript (f for center of cell face, and e for edge). To avoid solving for both $\mathbf{e}$ and $\mathbf{b}$, we can eliminate $\mathbf{e}$ by applying the relationship

$$\mathbf{e} = \mathbf{M}^{e-1}_\sigma \left(\mathbf{C}^\top \mathbf{M}^f_{\mu^{-1}}\mathbf{b} - \mathbf{s}_e \right). \tag{10}$$

The magnetic flux density field can then be solved for at every frequency by solving the equation

$$\left(\mathbf{C}\mathbf{M}^{e-1}_\sigma \mathbf{C}^\top \mathbf{M}^f_{\mu^{-1}} + i\omega \right)\mathbf{b} = \mathbf{s}_m + \mathbf{M}^{e-1}_\sigma \mathbf{M}^e \mathbf{s}_e. \tag{11}$$

In the time domain, the $i\omega\mathbf{b}$ term in Eq. (11) becomes $\frac{\partial \mathbf{b}}{\partial t}$, which can be discretized and solved using a backwards Euler as

$$\left(\mathbf{C}\mathbf{M}^{e-1}_\sigma \mathbf{C}^\top \mathbf{M}^f_{\mu^{-1}} \mathbf{b}^{n+1} + \frac{\mathbf{b}^{n+1} - \mathbf{b}^n}{\Delta t} \right) = \mathbf{s}^{n+1}_m + \mathbf{M}^{e-1}_\sigma \mathbf{M}^e \mathbf{s}^{n+1}_e \tag{12}$$

where n describes the field at the current time-step, $n+1$ describes the field at the next time-step, and Δt is the time-step length. Solving Eq. (12) for $\mathbf{b}^{n+1}$ gives the system

$$\left(\mathbf{I} + \Delta t \mathbf{C}\mathbf{M}^{e-1}_\sigma \mathbf{C}^\top \mathbf{M}^f_{\mu^{-1}} \right)\mathbf{b}^{n+1} = \mathbf{b}^n + \Delta t \left(\mathbf{s}^{n+1}_m + \mathbf{M}^{e-1}_\sigma \mathbf{M}^e \mathbf{s}^{n+1}_e \right) \tag{13}$$

for each time-step.

To implement the finite-volume method, we use the frequency and time-domain electromagnetics modules in SimPEG (Cockett et al., 2015; Heagy et al., 2017). For computational efficiency, the modeling uses an octree mesh with the greatest mesh refinement at the source location, along the air–earth interface (receiver locations), and at the reservoir depths.

5. Cross-dipole modeling results

The first scenario we model is an electric dipole source operating in the frequency domain. A dipole source induces both horizontal and vertical currents into the subsurface, leading the current to interact with 3D conductivity structure in the subsurface. This is opposed to the predominant way of using a surface TDEM loop which only induces horizontal currents in the subsurface, which makes the method less sensitive to 3D conductivity structures. Another advantage the dipole source has over a TDEM loop source is that the source has galvanic and inductive coupling to the ground, whereas TDEM relies solely on induction physics to drive current into the subsurface. The multiple modes of current supply allow for a more comprehensive sensitivity to the subsurface.

We model two cross-dipole sources in this section. The first is a cross centered at the injection site, and the second is offset from the

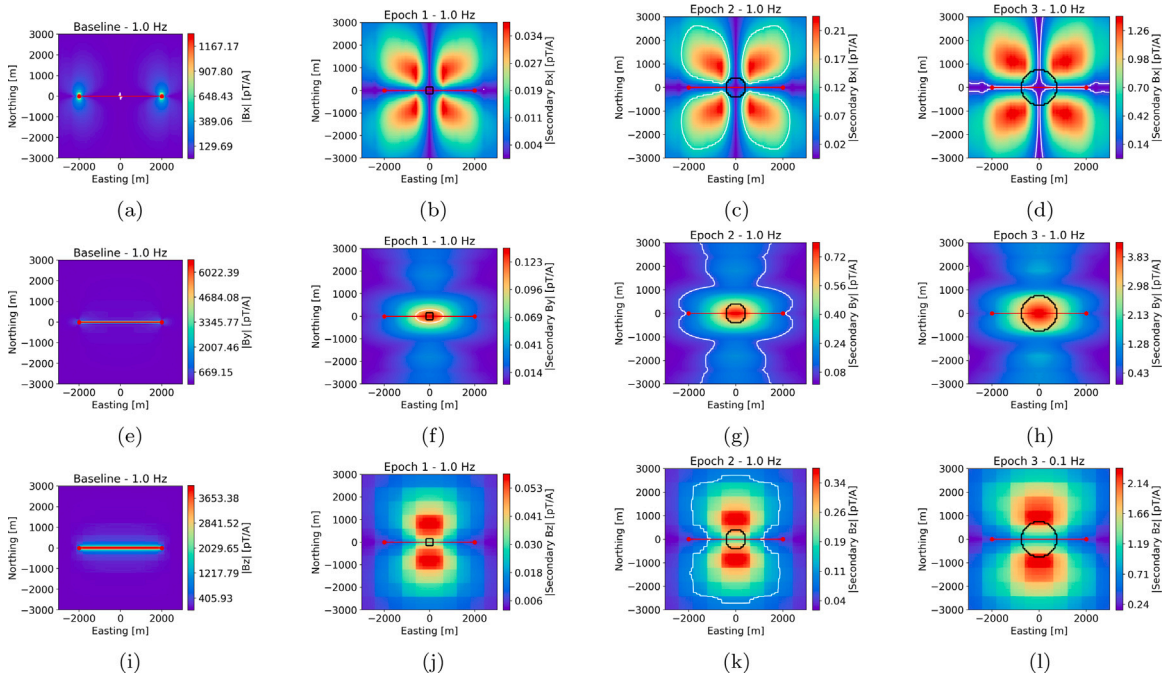

Fig. 5. Magnetic flux density from a 1.0 Hz dipole source. The resulting x-component (top), y-component (middle), and z-component (bottom) for the baseline (left), and secondary fields for each epoch (columns). Centered dipole source in red. White contour at 0.1 pT/A where applicable.

injection site. Both transmitters are approximately 4.5 km in length and oriented in the easting ($\hat{x}$) and northing ($\hat{y}$) directions. The receivers are placed on a 200 × 200 grid between −3000 m and 3000 m at the surface and measure the three primary components of the magnetic flux density. The transmitter operates at 0.1, 1.0, and 10.0 Hz respectively, and the fields are a combination of the two antenna that make up the cross-dipole source transmitting simultaneously.

5.1. Centered cross-dipole

To understand the response from a FDEM cross-dipole, we first analyze the response from a single dipole centered on the injection site. The resulting magnetic flux density at receivers for a source dipole operating at 1 Hz is shown in Fig. 5. Since the system is symmetric, any straight dipole through the center of the injection site will produce these field, albeit with the components rotated to reflect the orientation of the source. The x-component of the secondary field creates a symmetric "clover-leaf" pattern centered on the injection site. The y-component creates a "target-ring" pattern elongated in the direction of the transmitter dipole, and centered on the injection site. The z-component has two highs to the North and South of the transmitter. These highs in the data are a decent indicator of the extend of the CO_2 plume at depth. The magnitudes of the fields in this scenario are promising. In the first epoch, a transmitter of 10 A would be able to recover all but the lowest 20% of the signal for this specific receiver configuration. The magnitude of the signal increases in epochs 2 and 3, with the final epoch being able to be detected with unitary current.

The first cross-dipole we consider is centered on the injection site. The resulting magnetic flux density at receivers is shown in Fig. 6. Starting at epoch 1, the B-field anomaly is centered over the injection site with the field spreading primary in the northeast and southeast directions. Secondary lobes exist to the northwest and southeast. Even with the relatively small amount of injected CO_2, the amplitude of the signal is measurable for a transmitter current greater than 10 A for 1 Hz and below. At 10 Hz the signal is significantly weaker and localized to the injection site, but is still theoretically measurable for a transmitter above 10 A, but would likely require long stacking times and a low level of cultural noise at the site. Similar secondary fields are seen in the second and third epochs, with the fields growing in amplitude due to the increased CO_2 in the subsurface. The 10 Hz signal becomes stronger in these epochs, and now has an amplitude above the sensitivity floor of the receivers. The higher frequencies contain more fine-detail information about the CO_2 plume, so in the later epochs the higher frequencies can be used to track the CO_2 front and possibly detect leakage events.

The z-component of the magnetic flux density is shown in Fig. 7. This component shows highs in two quadrants of the survey area. Again, the overall shape of the field does not change with epoch, but the amplitude does increase with more subsurface CO_2. The signal strength is slightly lower than the y-component, but not by a significant amount that alters the results. We gain the same understanding as from the y-component – the z-component is measurable with a 10-A source and at frequencies 1 Hz and below; 10 Hz can used to monitor later epochs.

Given the results in Figs. 6 and 7, there are many possible useful configurations for the receivers to capture the maximum amount of information. The most useful is likely a cross shape pattern that is rotated 45° from the transmitter wires to capture the highs and lows in those directions. Another option is to run north–south or east–west receiver lines near the termination points of the dipoles.

5.2. Offset cross-dipole

In both components of the centered source the shape of secondary field does not change significantly due to the symmetry of the system being modeled. It may be possible to introduce asymmetry to track the edge of the CO_2 plume on the transmitter side by offsetting the dipoles from the injection site. The land directly surrounding the injection site may not be accessible, so it may be necessary to utilize other land to lay out the transmitter. To this end, we test offsetting each dipole in the previous experiment by 2 km from the injection site and repeat the modeling.

The first configuration we test to understand the FDEM cross-dipole response is using a single offset dipole and measuring the magnetic flux density at surface receivers. The resulting fields at 1 Hz are shown in Fig. 8. We choose to explore the response of the two dipoles that will compose the cross-dipole individually to understand their contribution

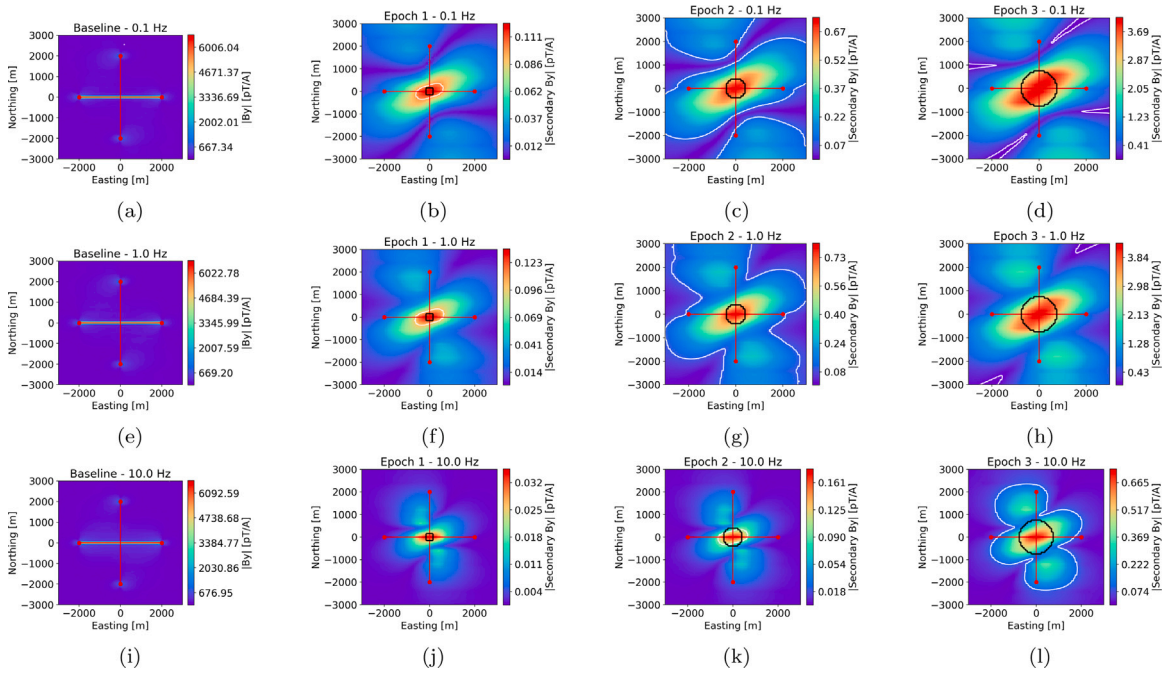

Fig. 6. Magnetic flux density y-component at 0.1 Hz (top), 1.0 Hz (middle), and 10 Hz (bottom) for the baseline (left), and secondary fields for each epoch (columns). Centered cross-dipole source in red. White contour at 0.1 pT/A where applicable.

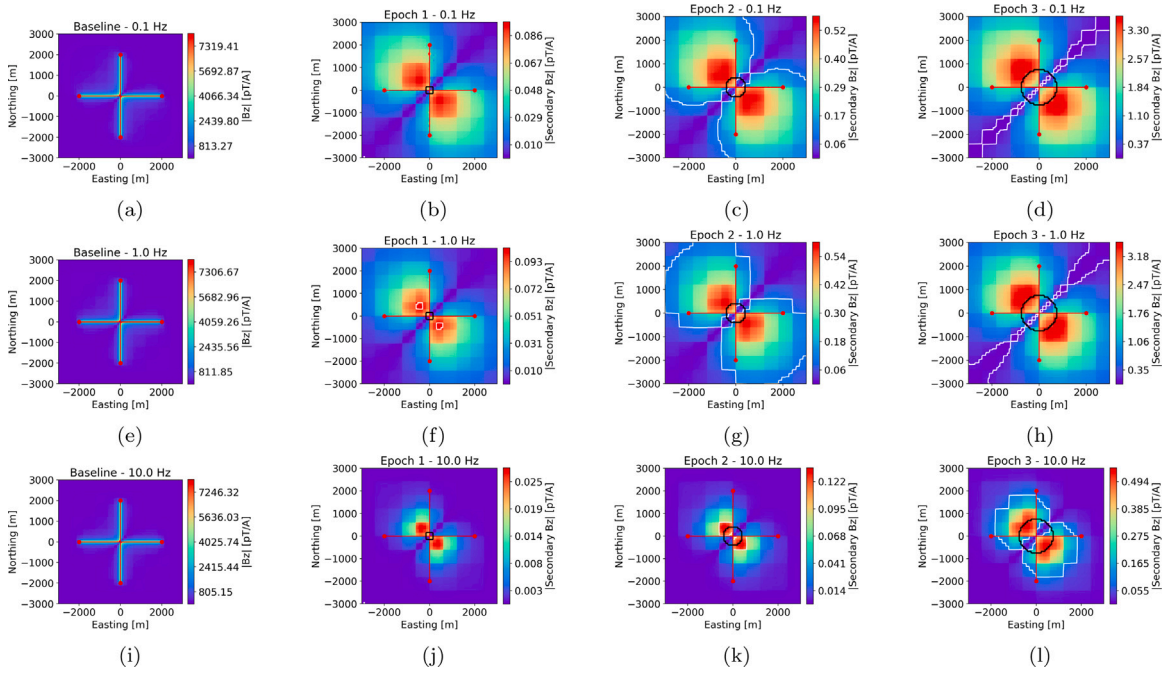

Fig. 7. Magnetic flux density z-component at 0.1 Hz (top), 1.0 Hz (middle), and 10 Hz (bottom) for the baseline (left), and secondary fields for each epoch (columns). Centered cross-dipole source in red. White contour at 0.1 pT/A where applicable.

to the cross-dipole. While only the y- and z-component of the secondary fields are shown, the symmetry of the system is such that the y-component of one transmitter is the rotated x-component of the other, and the z-component will be a rotation when considering the other transmitter. The response of these transmitters yields similar results in shape to the single centered dipole response. In epochs 2 and 3, the fields are secondary fields are stronger on the transmitter side of the injection plume, which makes sense due to more current being injected on that side. The amplitude of the secondary fields are about half as strong in the centered dipole case, meaning that the field can be detected with a transmitter of approximately 20 A. Overall, using a single FDEM dipole can be beneficial to monitoring efforts and produce fields that can aid in recovering the CO_2 plume at depth.

The y-component magnetic flux density field at surface receivers is seen in Fig. 9. The results of the secondary fields are similar in shape to the centered dipole source and are still centered on the CO_2 injection site. The amplitude of the fields are smaller due to the weaker primary field at the CO_2 plume from offsetting the source, but the values remain in the detectable range of with a source current of 10 A. By summing the results of the two transmitters, we introduce a

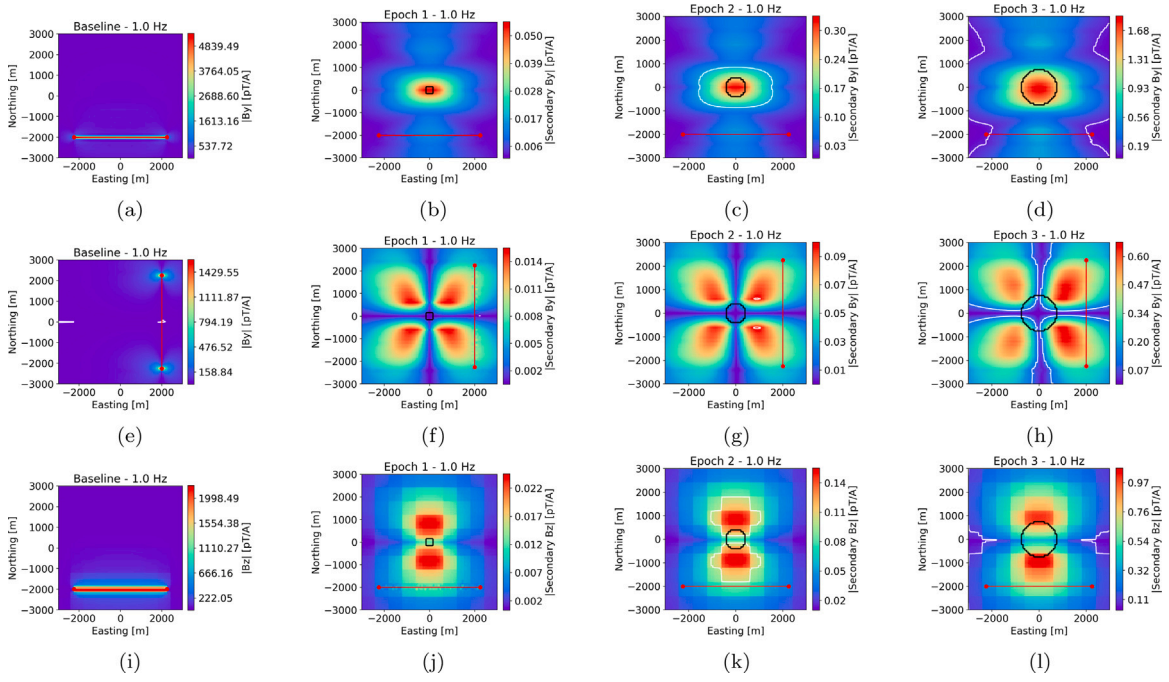

Fig. 8. Magnetic flux density from a 1.0 Hz dipole source. The resulting *y*-component for a dipole source to the south of the injection site (top), *y*-component for a dipole source to the east of the injection site (middle), and *z*-component for the dipole source in the south (bottom) for the baseline (left), and secondary fields for each epoch (columns). Offset dipole source in red. White contour at 0.1 pT/A where applicable.

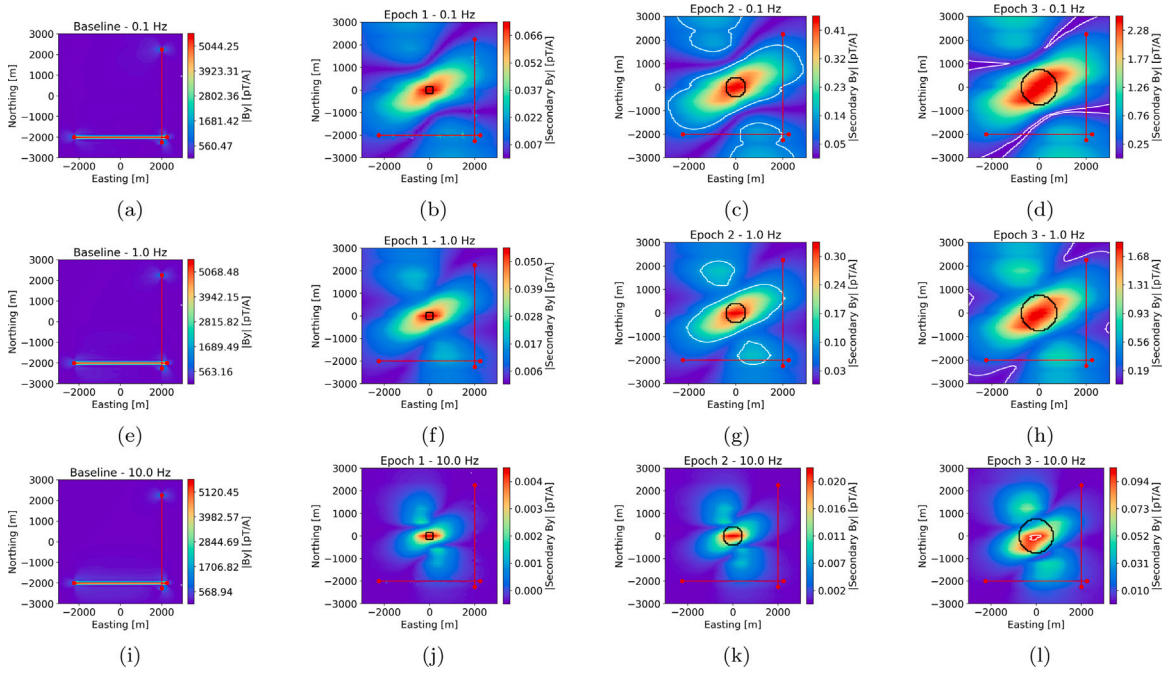

Fig. 9. Magnetic flux density *y*-component at 0.1 Hz (top), 1.0 Hz (middle), and 10 Hz (bottom) for the baseline (left), and secondary fields for each epoch (columns). Offset cross-dipole source in red. White contour at 0.1 pT/A where applicable.

virtual current from the southwest transmitter termination point to the northeast termination point and passes directly through the anomaly at depth. This allows for the anomaly to still be detected even if the transmitter is offset.

Fig. 10 shows the *z*-component of the magnetic flux density field at receivers. The magnitude of the secondary magnetic field shows two distinct highs at opposite ends of the CO_2 plume. Again, the response is measurable with a 10-A source current and at 1 Hz and below for the first epoch. The second and third epochs show that the plume response is measurable at 1 Hz and below for a unit transmitter. The third epoch also has potential to be measured by a transmitter of approximately 10 A and operating at 10 Hz.

Even though the transmitter has been offset, it is still beneficial for the receivers to be near injection site. In the case of ground-based surveys, the secondary field is captured by receivers laid out in a cross pattern, or eight-pointed star pattern centered on the injection site.

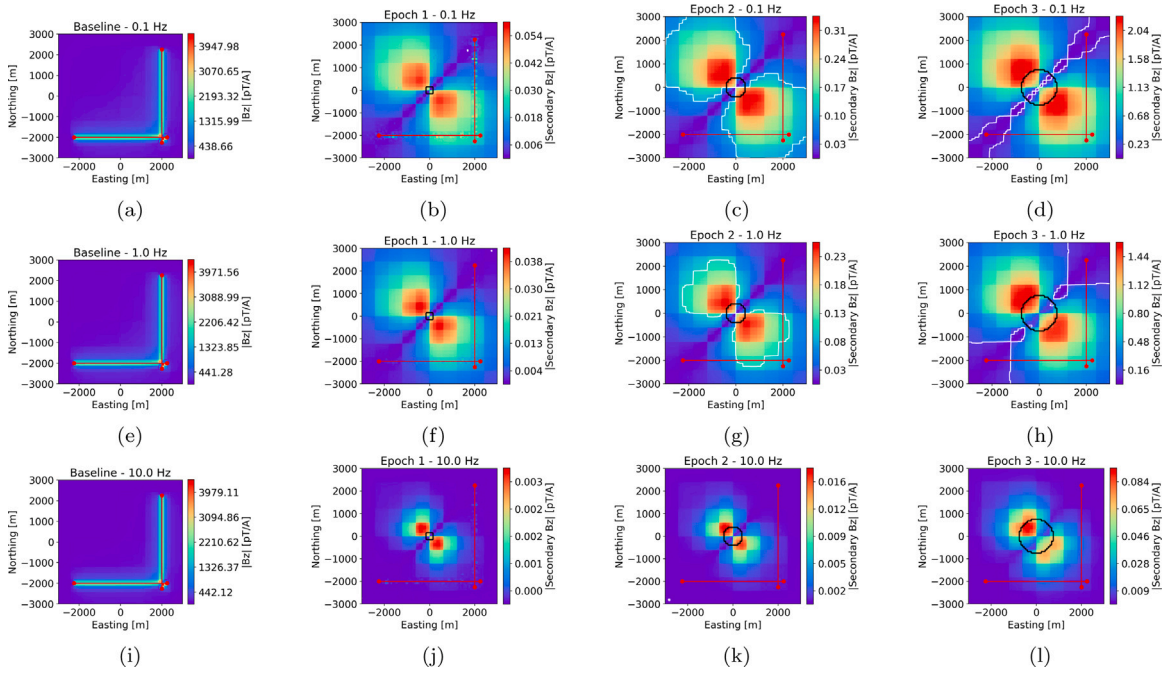

Fig. 10. Magnetic flux density z-component at 0.1 Hz (top), 1.0 Hz (middle), and 10 Hz (bottom) for the baseline (left), and secondary fields for each epoch (columns). Offset cross-dipole source in red. White contour at 0.1 pT/A where applicable.

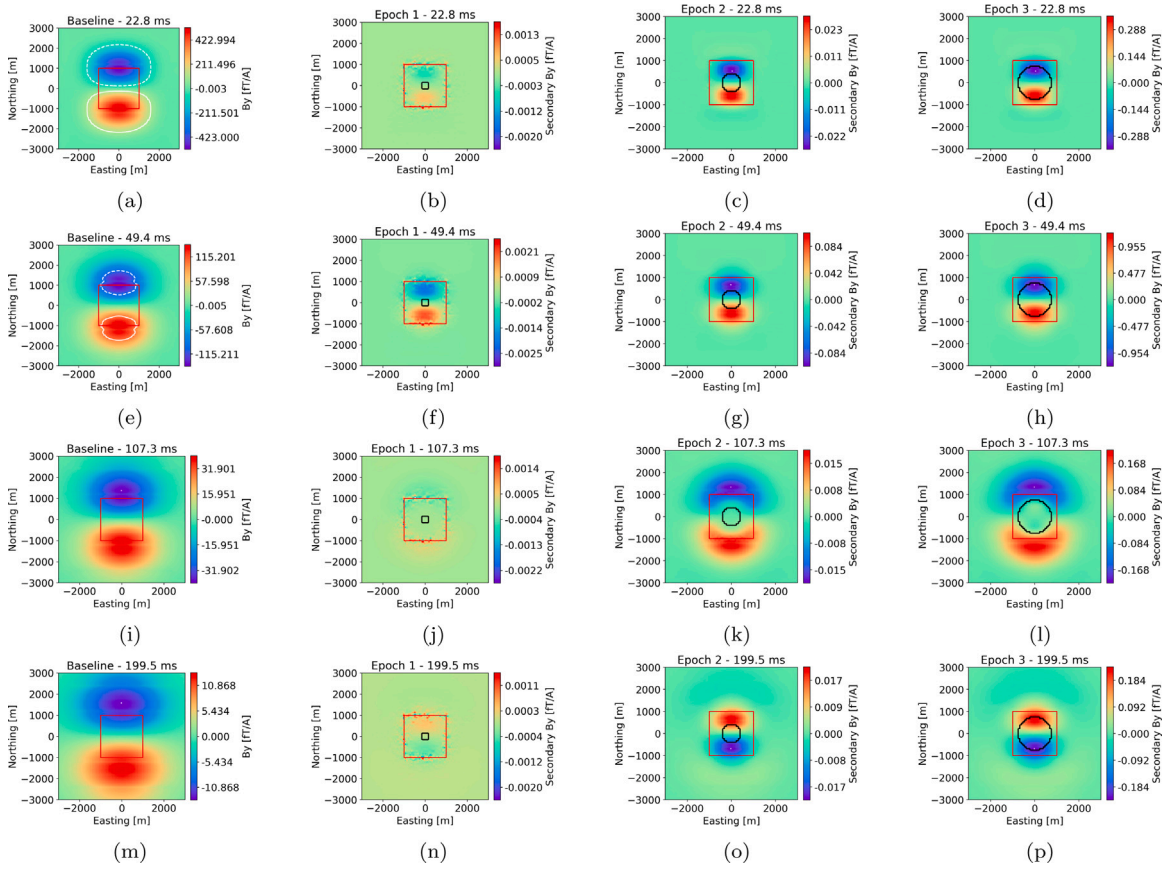

Fig. 11. Magnetic flux density y-component at different time slices (rows) for the baseline and secondary fields for each epoch (columns). Centered TDEM loop source in red. White contour at 0.1 pT/A where applicable.

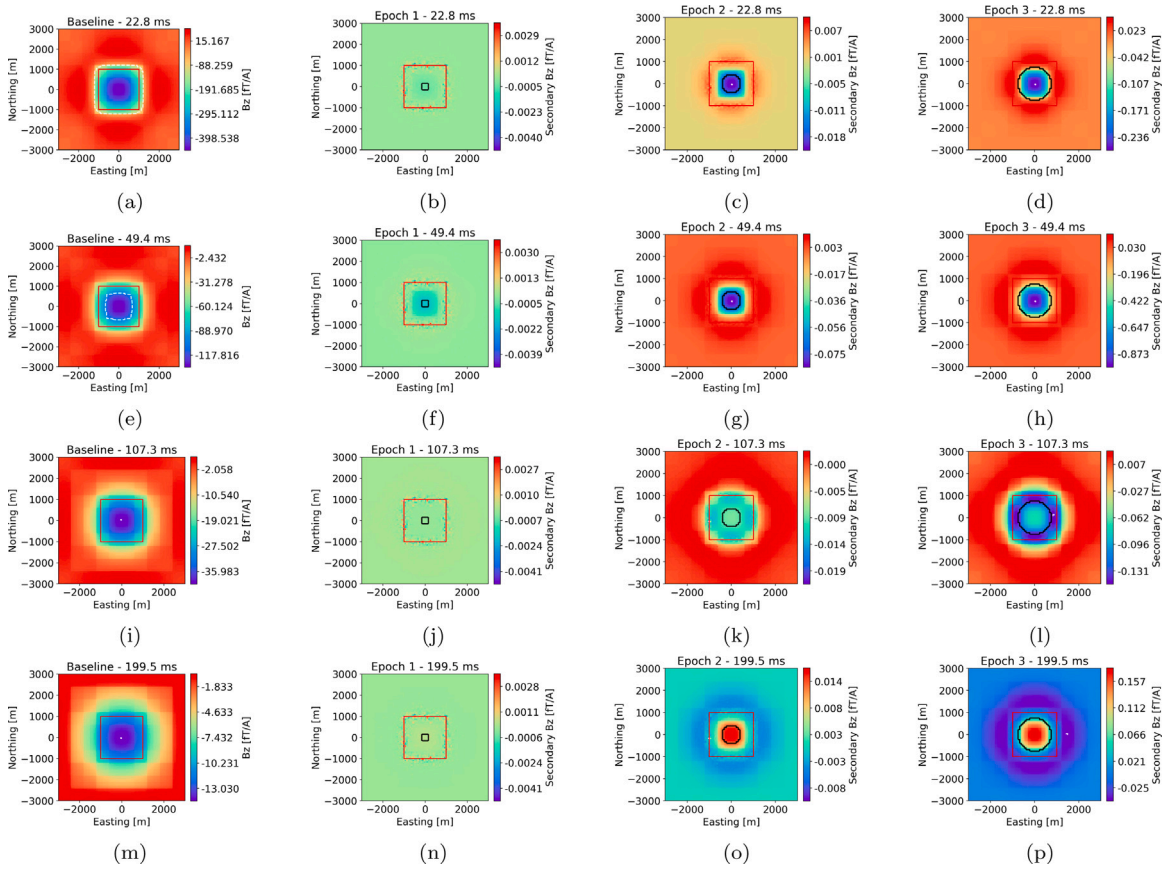

Fig. 12. Magnetic flux density z-component at different time slices (rows) for the baseline and secondary fields for each epoch (columns). Centered TDEM loop source in red. White contour at 0.1 pT/A where applicable.

6. TDEM loop modeling results

Next we evaluate using a time domain electromagnetics (TDEM) loop transmitter for monitoring a CO_2 plume. A TDEM transmitter loop has a few advantages over a FDEM dipole source. The advantages stem from the induction physics governing the TDEM loop transmitter. In short, the TDEM loop transmitter induces currents in the subsurface through Lenz's law of induction. The induced currents diffuse as "smoke rings" downward into the subsurface and create eddy currents around conductive bodies. The eddy currents then generate a magnetic field which can be measured at receiver locations (Nabighian and Macnae, 1991). In the case of CO_2 monitoring, instead of investigating a conductive body, we treat the saline reservoir as a conductor that becomes increasingly more resistive as the CO_2 is injected.

Since the process of a TDEM loop is purely inductive, the transmitter does not need to be galvanically coupled with the ground like in the above cross-dipole case. This allows for one to use airborne transmitters to cover large survey areas. The strength of the induced current in a TDEM survey is tied to how fast the transmitter can shut off, with faster turn-off times yielding higher induced currents. Each transmitter will have a unique turn-off time based on the survey configuration and electronics, and it is important to account for in the modeling. A drawback of a TDEM loop transmitter is that only horizontal currents are induced into the subsurface in the CO_2 model in this study, whereas the cross-dipole source generates horizontal and vertical currents. Vertical current allow for better mapping of horizontal structure and horizontal currents allow for better mapper of vertical structure, so by missing a component of the current, it may be increasingly difficult to detect the CO_2 plume. So while TDEM loop surveys are more mobile due to induction physics, the consequences of the physics may prevent the success of the method at the Kemper site.

The following modeling results use the same mesh and conductivity models as the cross-dipole case. The transmitter waveform is a linear ramp-off over 300 μs. The receivers measure the three component magnetic flux density at times logarithmically spaced between 80 μs and 250 ms measured from the end of the ramp-off. Standard TDEM loop surveys stop recording at the receivers after about 20 ms, however since SQUID magnetometers have low levels of internal noise, it is possible to recover usable signal into the hundreds of milliseconds. This allows the smoke ring to travel further into the subsurface and therefore we obtain information about the deeper subsurface by recording for longer periods of time. For the investigation in this paper, we consider the receiver times at approximately 22.8, 49.4, 107.3, and 199.5 ms.

6.1. Concentric loop

The first TDEM transmitter loop we consider is a square loop with 2 km side length centered directly over the injection site. The y-component of the magnetic field is shown in Fig. 11, and the z-component in Fig. 12. Note the colorbar scale has changed to fT/A from pT/A in the cross-dipole case. Immediately we notice that the secondary fields are far below the detection threshold as above, however, we still may be able to gain insight from the shape of the recorded fields.

The most interesting feature of the modeling at this stage is the polarity flip that occurs between the 107 and 199 ms time-steps. In a TDEM loop survey, there are two sources of secondary signal, the first is the induced smoke-ring, and the second is the eddy currents induced by the time-varying magnetic field. In the first three times the secondary signal from the smoke ring dominates, resulting in a pattern that diffuses outward at the surface with time. In the final time, the smoke-ring signal diminishes and the eddy-current signal begins to

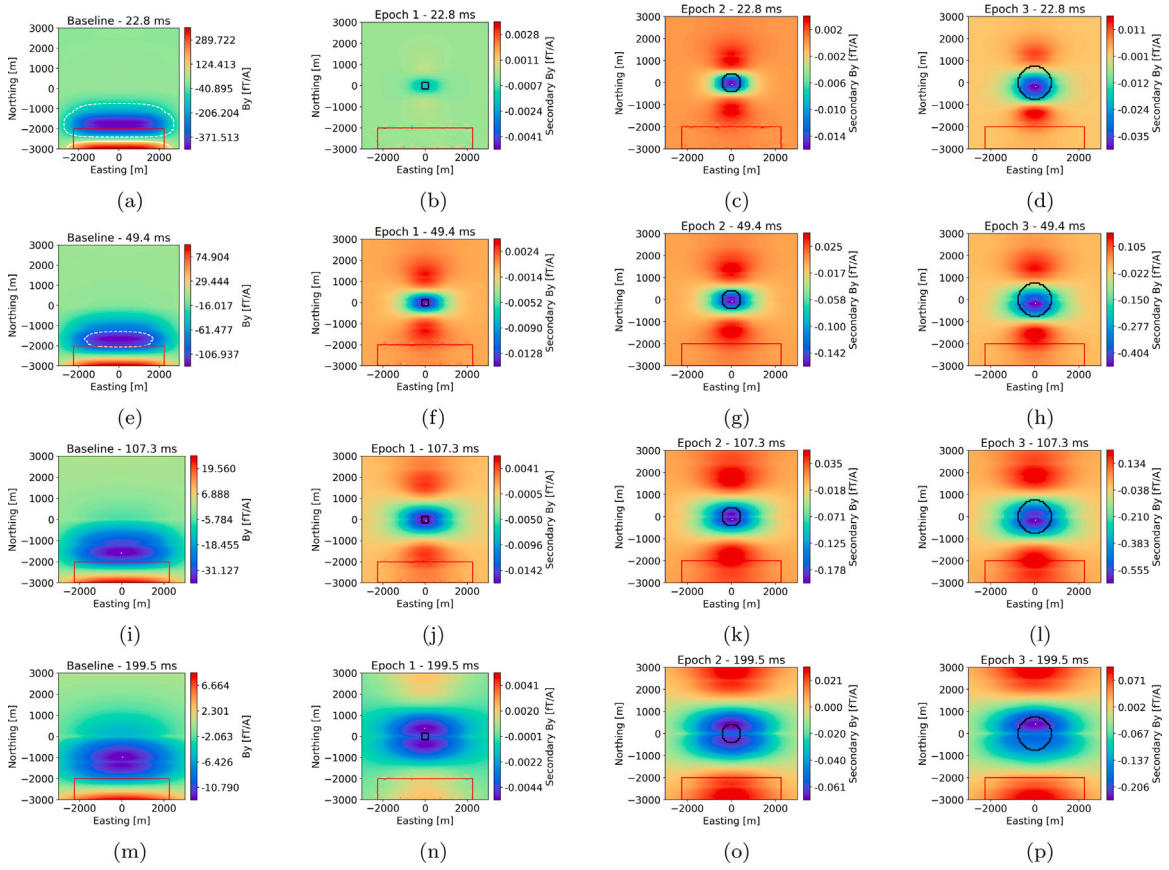

Fig. 13. Magnetic flux density y-component at different time slices (rows) for the baseline and secondary fields for each epoch (columns). Offset TDEM loop source in red. White contour at 0.1 pT/A where applicable.

dominates with the flipped polarity due to Lenz's law. Since the eddy current signal is dominating in the late time, the secondary magnetic field give a good indication of the horizontal location of the body at depth. So if one could measure the magnetic field into the sub fT/A range, TDEM loops may be a useful transmitter.

6.2. Offset loop

Another option is to create a larger loop with a higher dipole moment and offset the loop to get a different polarization of the CO_2 plume by the source currents. We offset the loop by 2.5 km to the south of the injection site, and extend the loop to be 4.5 × 1.0 km in dimensions.

Fig. 13 shows the y-component of the secondary field and Fig. 14 shows the z-component. As with the centered loop, the secondary field is too small to reasonably measure at the receiver locations. The shape of the secondary fields are consistent with time, and there are no polarity flips as in the centered loop case.

6.3. Buried receivers

The subsfurface at the Kemper site is fairly conductive and much of the signal from the transmitter dissipates by traveling through the subsurface to the CO_2 plume, and then back to the surface to be measured at the receivers. We can half the distance the signal needs to travel by burying receivers and seeing if that is enough to overcome the falloff in the signal. We bury the plane of receivers at 800 m, just above the first reservoir layer where CO_2 is injected. In reality the receivers would be placed in boreholes in this scenario, so the data would be collected at the handful of points instead of a plane. However, by looking at the data on the plane we are able to determine where it is most advantageous to place receivers if given the opportunity.

Fig. 15 shows the y- and z-components at depth for the centered TDEM loop. The amplitude of the secondary field is approximately two orders of magnitude higher than when the receivers are placed on the surface. The spacial extent of the secondary field is also more localized to the CO_2 plume. With a sufficiently large transmitter current, approximately 50 A, the secondary field for the second and third epochs is raised to just above the sensitivity floor. To detect the secondary signal, placing the receiver near the suspected edge of the plume gives a sufficient response.

The secondary fields for the offset loop are shown in Fig. 16. Again, the amplitude of the secondary field has increased by approximately two orders of magnitude. The y-component is localized to the CO_2 plume and the z-component has highs at the boundaries of the plume. The amplitude of the signal has increased, however to measure the secondary field, a transmitter of 100 A or greater would be required to overcome the sensitivity floor of the equipment. Receivers in this scenario would be best placed either between the transmitter and the injection site, or on the far side of the injection site past where the CO_2 plume is expected to expand. As the CO_2 plume expands towards the receiver, the amplitude of the z-component of the secondary field would increase and effectively serve as a way to monitor the CO_2 expanding from the injection site to the buried receiver.

7. Proposed surveys at the Kemper CarbonSAFE site

The above modeling results suggest that it is most beneficial to have transmitters offset from the injection site, and have magnetic field receivers cross over the boundaries of the CO_2 plume. The size of the transmitters are common for exploration in undeveloped areas, but land

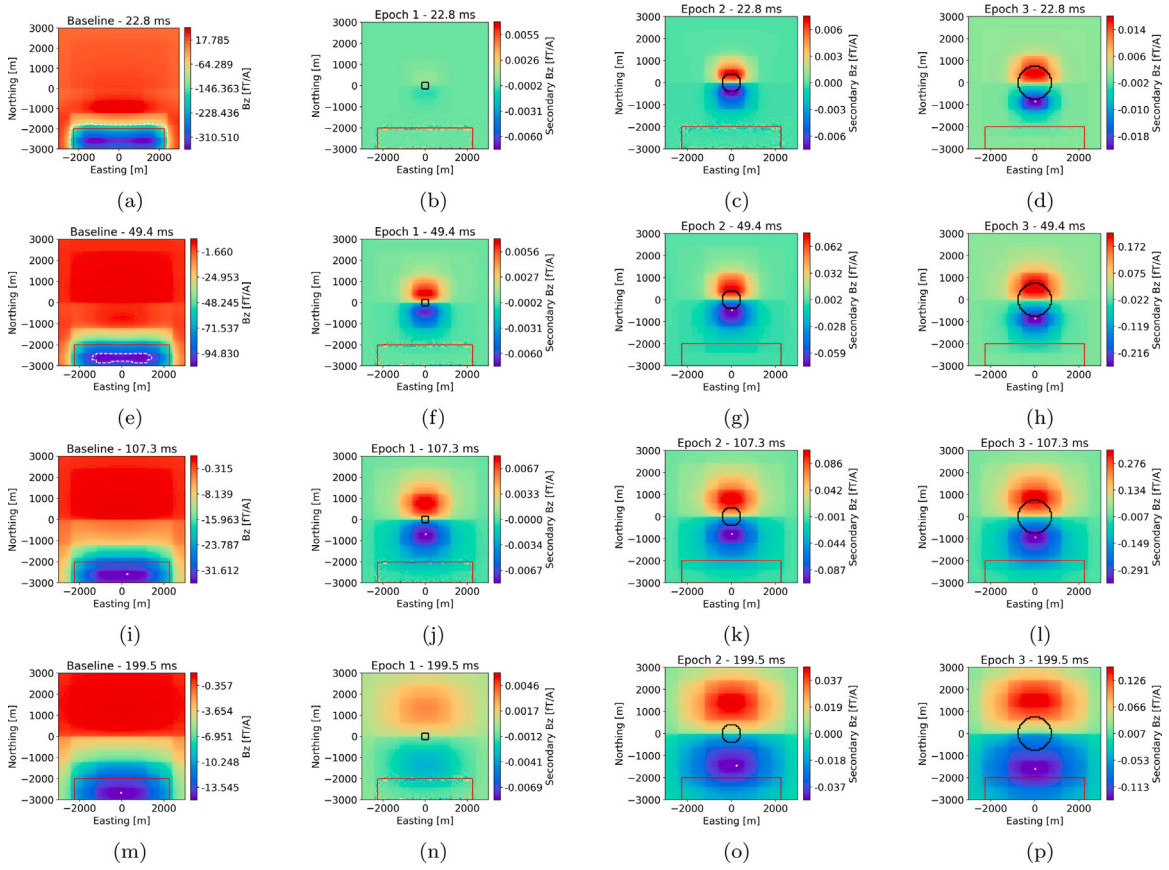

Fig. 14. Magnetic flux density z-component at different time slices (rows) for the baseline and secondary fields for each epoch (columns). Offset TDEM loop source in red. White contour at 0.1 pT/A where applicable.

access and permitting issues in more developed areas may limit urban exploration. Kemper is one such area where the transmitter locations are limited, so as a finally experiment, we model the cross-dipole source in a configuration that is compact to a single parcel of land to the southeast of a theoretical injection site.

The y-component of the magnetic flux density is shown in Fig. 17. Surprisingly, the shape of the secondary fields are similar to the cases with the long transmitter wires, however with a slight bias towards the cross-dipole transmitter. The amplitude of the secondary field is above the sensitivity floor of the SQUID magnetometers and a transmitter of 10 A for 1 Hz and below. A transmitter of approximately 50 A is able to resolve the secondary field at 10 Hz.

Fig. 18 shows the z-component of the magnetic flux density. Again, we see the pattern mirror that found with the long transmitter wire. In the third epoch, the secondary field is biased towards the transmitter side and illuminates the southeastern edge of the CO_2 plume. Overall, the smaller transmitter is able to produce a measurable change due to CO_2 injection, but only once a certain amount has been injected (in this case, the amount representative of 3 years). While this transmitter configuration is not ideal, due to local noise, it does show that only a relatively small surface footprint for the transmitter is required for monitoring purposes.

8. Discussion

While the results suggest that a cross-dipole transmitter is appropriate at the Kemper site, there are still unknowns that are impossible to quantify without a field study. The cultural noise is the main concern at the site. If the cultural noise is low enough, the time-lapse signal will still be measurable, however high levels of cultural noise will overpower the time-lapse signal. Satellite images show that the Kemper site is located in a fairly rural area of Mississippi, which is advantageous from a noise perspective, but the presence of the power station to the north of the proposed injection site increases the cultural noise in the area. Any noise contaminating the signal of interest may be filtered out and attenuated without losing subsurface information using techniques such as aerial averaging, smart stacking, remote stations, and modeling infrastructure. However, the effectiveness of such techniques are largely unknown until field data is collected and analyzed.

Another unknown to consider is the CO_2 saturation used in the modeling. While we used a constant 80% saturation value, a more realistic model would be the product of reservoir simulations and have a variable saturation that is highest at the site of injection and lowest towards the edges of the plume. Producing a realistic model of saturation is highly dependent on the reservoir properties, injection rate, and pressure regime of the system.

Similarly, sources and characteristics of time-lapse noise were not investigated due to lack of available information. The EM methods are sensitive to the ground conductivity, so changes in the near-surface conductivity due to groundwater movement or saturation between surveys can have significant effects on the time-lapse signal. Development of infrastructure between surveys can also introduce sources of time-lapse noise, such as additional power lines, or grounded wires, that interfere with the survey. One wants to repeat the survey to the best of their ability to reduce errors from survey geometry, so if the survey site becomes inaccessible in the future, that can also have an impact on being able to successfully monitor the CO_2 movement of the site. Thankfully, the shape of the secondary field is largely unaffected by the cross-dipole transmitter location, so it may be possible to monitor in a time-lapse mode with an arbitrary transmitter for each epoch and airborne magnetic field receivers.

Any collected time-lapse data needs to have methods of interpretation and inversion applied. Without such methods, it is difficult to know

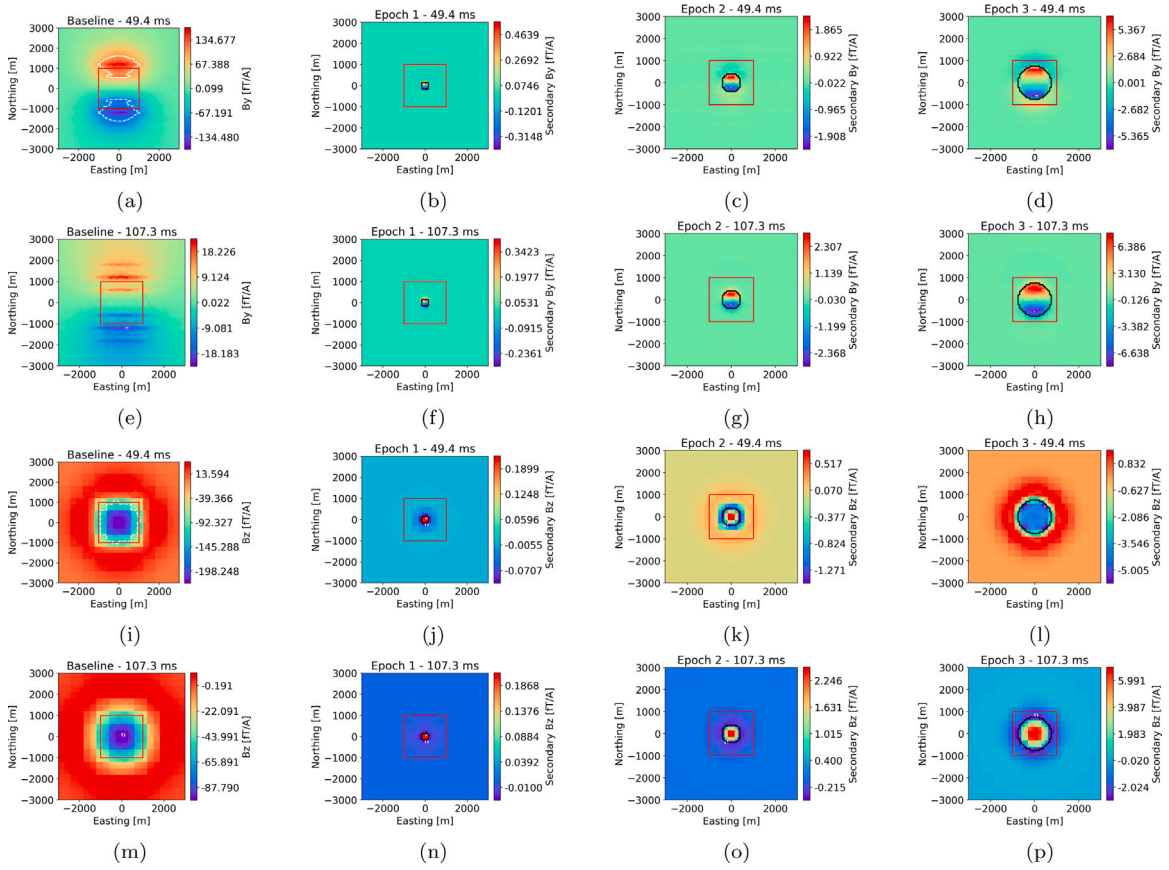

Fig. 15. Magnetic flux density y- and z-component at buried receivers at different time slices (rows) for the baseline and secondary fields for each epoch (columns). Centered TDEM loop source in red. White contour at 0.1 pT/A where applicable.

what the time-lapse signal represents in the subsurface. For instance, in the models of Kemper, it is unknown if the data represents all three injection zones, or if there is a bias towards a specific layer. It is likely that only the shallowest layer is being imaged sufficiently due to the conductivity of the reservoir layers above the lower layers attenuating the EM signal. However, this remains an open area of research.

9. Conclusion

The cross-dipole FDEM results suggest that with a transmitter operating at 1 Hz and below, and carrying 1 A of current, is able to monitor the CO_2 plume in the second and third epochs. It is possible to monitor the CO_2 in the first epoch with a transmitter of approximately 10 A and stronger. The transmitter centered over the CO_2 plume injection site gives the strongest response, where the offset transmitters give a weaker, but still measurable, response. It may also be possible to operate the cross-dipole in a time-domain mode to gain further insights to the subsurface CO_2 plume.

While the TDEM loop produces secondary field patterns that would be beneficial for monitoring efforts, the strength of the secondary field does not fall in the measurable range. A transmitter of approximately 1000 A may be able to overcome the 0.1 pT sensitivity floor in the second and third epochs, but such a transmitter does not currently exist. If the receivers are buried, a transmitter of approximately 100 A gives a secondary field above the sensitivity floor, but this is still not ideal due to the limited locations buried receivers can exist. So while it may be possible to monitor the Kemper site with a TDEM loop, the signal strength and ability to have source and receiver above ground using the cross-dipole source outweighs any potential monitoring benefits of using a TDEM loop.

For a spatially limited survey with a short cross-dipole transmitter offset from the injection site, the recovered signal mirrors that of the larger transmitters. The secondary signal decreases as expected from the reduced dipole moment of the transmitter, however, the signal is still measurable with a current of approximately 10 A and frequencies of 1 Hz and below.

In all cases, the location of the transmitters does not have a significant impact of the shape of the secondary fields. To recover the shape of the secondary fields, receiver lines should be placed such that they cross the center of the injection site, such as in a cross shape or eight pointed-star. The lengths of the receiver lines should be approximately 4 km each, with variable station spacing that is closer near the injection site, or estimated CO_2 plume boundary, and farther towards the line ends.

CRediT authorship contribution statement

Colton Kohnke: Conceptualization, Software, Validation, Formal analysis, Investigation, Data curation, Writing – original draft, Writing – review & editing, Visualization. **Yaoguo Li:** Conceptualization, Resources, Supervision, Writing – review & editing, Funding acquisition, Project administration. **Richard W. Hammack:** Conceptualization, Resources, Supervision, Writing – review & editing, Funding acquisition, Project administration. **David Alumbaugh:** Conceptualization, Writing – review & editing.

Declaration of competing interest

The authors declare the following financial interests/personal relationships which may be considered as potential competing interests: Colton Kohnke reports financial support, article publishing charges,

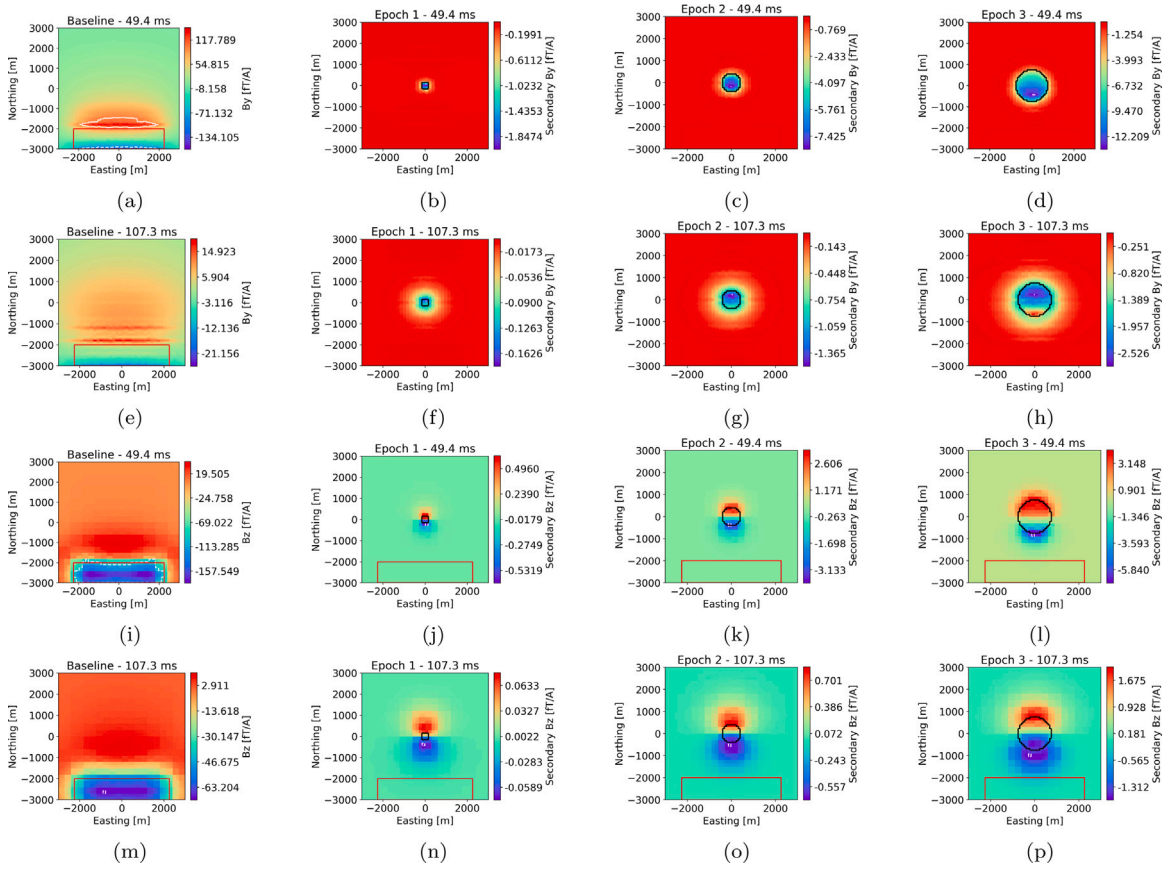

Fig. 16. Magnetic flux density *y*- and *z*-component at buried receivers at different time slices (rows) for the baseline and secondary fields for each epoch (columns). Offset TDEM loop source in red. White contour at 0.1 pT/A where applicable.

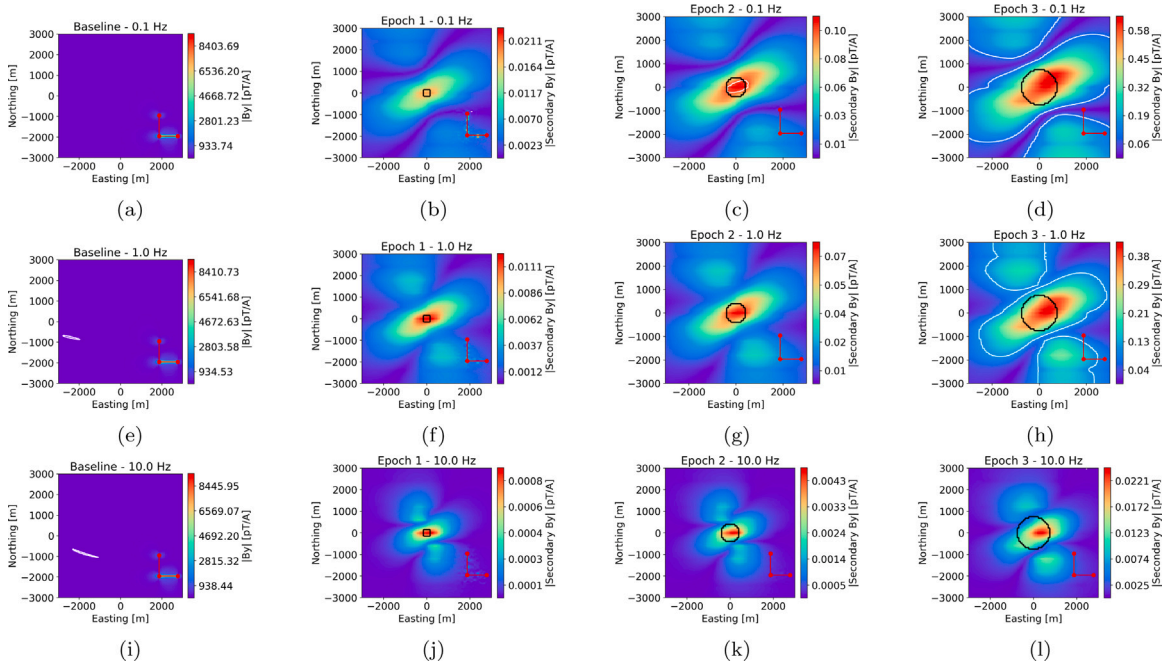

Fig. 17. Magnetic flux density *y*-component at 0.1 Hz (top), 1.0 Hz (middle), and 10 Hz (bottom) for the baseline (left), and secondary fields for each epoch (columns 2–4). Space-limited cross-dipole source in red. White contour at 0.1 pT/A where applicable.

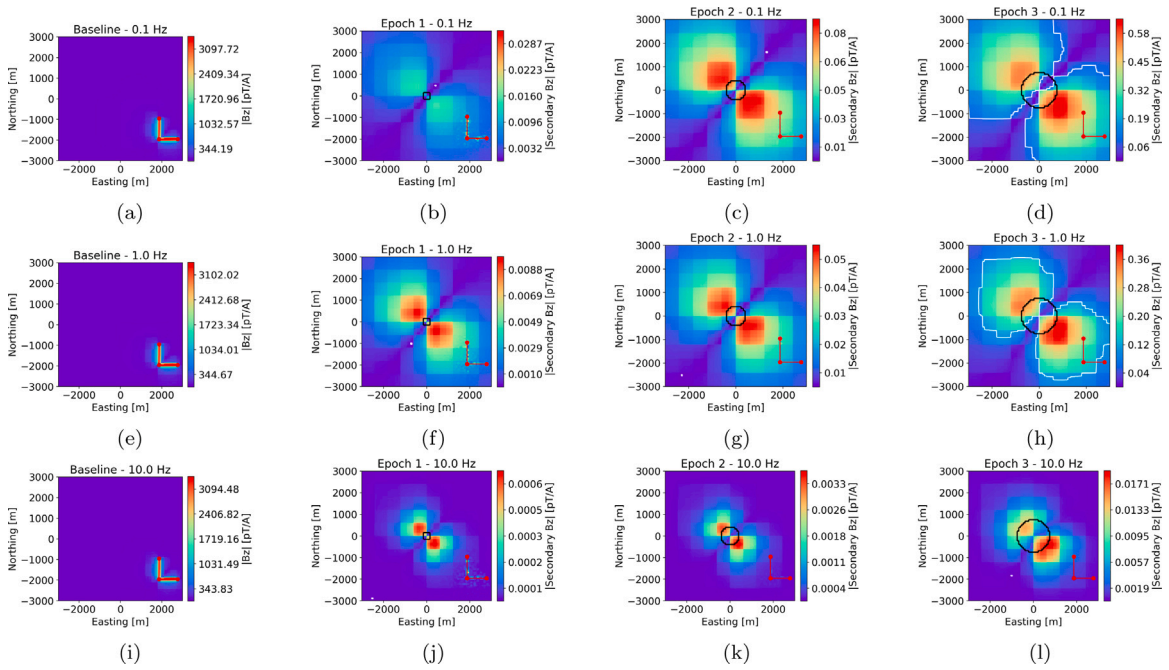

Fig. 18. Magnetic flux density z-component at 0.1 Hz (top), 1.0 Hz (middle), and 10 Hz (bottom) for the baseline (left), and secondary fields for each epoch (columns 2–4). Space-limited cross-dipole source in red. White contour at 0.1 pT/A where applicable.

and travel were provided by National Energy Technology Laboratory. Yaoguo Li reports financial support was provided by National Energy Technology Laboratory.

Data availability

Data will be made available on request

Acknowledgments

This project was funded by the Department of Energy, National Energy Technology Laboratory an agency of the United States Government, through a support contract with Leidos Research Support Team (LRST). Neither the United States Government nor any agency thereof, nor any of their employees, nor LRST, nor any of their employees, makes any warranty, express or implied, or assumes any legal liability or responsibility for the accuracy, completeness, or usefulness of any information, apparatus, product, or process disclosed, or represents that its use would not infringe privately owned rights. Reference herein to any specific commercial product, process, or service by trade name, trademark, manufacturer, or otherwise does not necessarily constitute or imply its endorsement, recommendation, or favoring by the United States Government or any agency thereof. The views and opinions of authors expressed herein do not necessarily state or reflect those of the United States Government or any agency thereof.

The authors also thank the SimPEG project for the finite volume electromagnetic modeling codes (Heagy et al., 2017).

Formatting of funding sources

This project was funded by the Department of Energy, National Energy Technology Laboratory an agency of the United States Government, through a support contract with Leidos Research Support Team (LRST) awarded to the Colorado School of Mines Center for Gravity, Electrical, and Magnetic Studies.

References

Arai, E., 2003. Development of a TDEM data acquisition system based on a SQUID magnetometer for mineral exploration. TEION KOGAKU (J. Cryog. Soc. Jpn.) 38 (9), 501–508.

Archie, G., 1942. The electrical resistivity log as an aid in determining some reservoir characteristics. Trans. AIME 146 (01), 54–62.

Ayani, M., Grana, D., MacGregor, L., Mallick, S., 2019. Sensitivity analysis of marine controlled source electromagnetic data in CO2 monitoring of the Johansen Formation. In: SEG Technical Program Expanded Abstracts 2019. Society of Exploration Geophysicists, pp. 1130–1134.

Barajas-Olalde, C., Davydycheva, S., Hanstein, T., Laudal, D., Martinez, Y., MacLennan, K., Mikula, S., Adams, D.C., Klapperich, R.J., Peck, W.D., Strack, K., 2021. Using controlled-source electromagnetic (CSEM) for CO2 storage monitoring in the North Dakota CarbonSAFE project. In: First International Meeting for Applied Geoscience & Energy Expanded Abstracts. Society of Exploration Geophysicists, pp. 503–507.

Beka, T.I., Senger, K., Autio, U.A., Smirnov, M., Birkelund, Y., 2017. Integrated electromagnetic data investigation of a Mesozoic CO2 storage target reservoir-cap-rock succession, Svalbard. J. Appl. Geophys. 136, 417–430.

Benson, S., Hoversten, G., Gasperikova, E., Haines, M., 2005. Monitoring protocols and life-cycle costs for geologic storage of carbon dioxide. In: Greenhouse Gas Control Technologies 7. Elsevier, pp. 1259–1264.

Bhuyian, A.H., Ghaderi, A., Landrø, M., 2011. CSEM sensitivity study of CO2 layers with uniform versus patchy saturation distributions. In: SEG Technical Program Expanded Abstracts 2011. Society of Exploration Geophysicists, pp. 655–659.

Börner, J.H., Spitzer, K., 2013. Monitoring of CO2 sequestration and leakage using borehole transient electromagnetics and the DC resistivity method: A 3D feasibility study incorporating realistic geological scenarios. In: SEG Technical Program Expanded Abstracts 2013. Society of Exploration Geophysicists, pp. 4461–4465.

Börner, J.H., Wang, F., Weißflog, J., Bär, M., Görz, I., Spitzer, K., 2015. Multi-method virtual electromagnetic experiments for developing suitable monitoring designs: A fictitious CO2 sequestration scenario in Northern Germany. Geophys. Prospect. 63 (6), 1430–1449.

Brown, B.W., 1960. Geologic Study along Highway 16 from Alabama Line to Canton, Mississippi. Technical report, Mississippi Geological Survey.

Cockett, R., Kang, S., Heagy, L.J., Pidlisecky, A., Oldenburg, D.W., 2015. SimPEG: An open source framework for simulation and gradient based parameter estimation in geophysical applications. Comput. Geosci. 85, 142–154.

Dockery III, D.T., Thompson, D.E., 2016. The Geology of Mississippi. University Press of Mississippi, p. 751.

Gasperikova, E., Hoversten, G.M., 2006. A feasibility study of nonseismic geophysical methods for monitoring geologic CO2 sequestration. Lead. Edge 25 (10), 1282–1288.

Heagy, L.J., Cockett, R., Kang, S., Rosenkjaer, G.K., Oldenburg, D.W., 2017. A framework for simulation and inversion in electromagnetics. Comput. Geosci. 107 (June), 1–19.

Hoversten, G., Gasperikova, E., 2005. Non-seismic geophysical approaches to monitoring. In: Carbon Dioxide Capture for Storage in Deep Geologic Formations, Vol. 2. Elsevier, pp. 1071–1112, 23.

Hughes, R.J., 1958. Kemper County Geology. Technical report, Mississippi State Geologic Survey.

Kang, S., Seol, S.J., Byun, J., 2012. mCSEM inversion for CO2 sequestration monitoring at a deep brine aquifer in a shallow sea. In: SEG Technical Program Expanded Abstracts 2012. Society of Exploration Geophysicists, pp. 1–5.

Keller, G.V., 1988. Rock and mineral properties. In: Electromagnetic Methods in Applied Geophysics, Vol. 1. Society of Exploration Geophysicists, pp. 12–51.

Klara, S.M., Cohen, K., Byrer, C., Srivastava, R.D., 2004. The role of geophysics in developing strategies for CO2 sequestration in geologic formations. In: Symposium on the Application of Geophysics to Engineering and Environmental Problems 2004. Environment and Engineering Geophysical Society, pp. 283–296.

Krahenbuhl, R.A., Li, Y., McAliley, W.A., Moodie, N., Irons, T., Bloss, B.R., 2019. Integrated model construction for CO2-EOR monitoring via charged-wellbore casing controlled-source electromagnetics. In: SEG Technical Program Expanded Abstracts 2019. Society of Exploration Geophysicists, pp. 4908–4912.

MacLennan, K., 2022. Monitoring CO2 storage using well-casing source electromagnetics. Lead. Edge 41 (2), 107–113.

McAliley, W.A., Bloss, B.R., Irons, T., Moodie, N., Krahenbuhl, R., Li, Y., 2019. Analysis of land-based CSEM data for CO2 monitoring at Bell Creek, MT. In: SEG Technical Program Expanded Abstracts 2019. Society of Exploration Geophysicists, pp. 1039–1044.

Nabighian, M.N., Macnae, J.C., 1991. 6. Time domain electromagnetic prospecting methods. In: Electromagnetic Methods in Applied Geophysics. Society of Exploration Geophysicists, pp. 427–520.

Onishi, K., Ishikawa, Y., Yamada, Y., Matsuoka, T., 2006. Measuring electric resistivity of rock specimens injected with gas, liquid and supercritical CO 2. In: SEG Technical Program Expanded Abstracts 2006. Society of Exploration Geophysicists, pp. 1480–1484.

Palacky, G.J., 1988. Resistivity characteristics of geologic targets. In: Electromagnetic Methods in Applied Geophysics. Society of Exploration Geophysicists, pp. 52–129.

Puzyrev, V., 2019. Deep learning electromagnetic inversion with convolutional neural networks. Geophys. J. Int. 218 (2), 817–832.

Riestenberg, D., 2018. CarbonSAFE: Establishing an Early CO2 Storage Complex in Kemper County, Mississippi: Project ECO2S. OSTI.

Smith, E., Morris, J., Kheshgi, H., Teletzke, G., Herzog, H., Paltsev, S., 2021. The cost of CO2 transport and storage in global integrated assessment modeling. Int. J. Greenh. Gas Control 109, 103367.

Stoll, J.B., 2021. Advances and future trends in drone-borne geophysics. In: First International Meeting for Applied Geoscience & Energy Expanded Abstracts. Society of Exploration Geophysicists, pp. 3053–3057.

Streich, R., Becken, M., Ritter, O., 2010. Imaging of CO2 storage sites, geothermal reservoirs, and gas shales using controlled-source magnetotellurics: Modeling studies. Geochemistry 70 (SUPPL. 3), 63–75.

Zhang, Z.F., White, S.K., White, M.D., 2015. Delineating the horizontal plume extent and CO2 distribution at geologic sequestration sites. Int. J. Greenh. Gas Control 43, 141–148.

Zhdanov, M.S., Endo, M., Black, N., Spangler, L., Fairweather, S., Hibbs, A., Eiskamp, G.A., Will, R., 2013. Feasibility study of electromagnetic monitoring of CO2 sequestration in deep reservoirs. In: SEG Technical Program Expanded Abstracts 2013. Society of Exploration Geophysicists, pp. 2417–2421.

Zhou, Q., Birkholzer, J.T., Mehnert, E., Lin, Y.-F., Zhang, K., 2009. Modeling basin- and plume-scale processes of CO2 storage for full-scale deployment. Ground Water 48 (4), 494–514.